APPENDIX A

Sensor Calibration Using a Michelson Laser Interferometer

A.1 Background

Three eddy-current sensors (eddyNCDT3700 from Micro-Epsilon) were used to measure displacements of flexure hinges and the 3-RRR micro-motion stage in this thesis. These sensors provide a measurement range of 1000μm which corresponds to a voltage range of approximately 10V (see Figures B.1 to B.3). However, the displacement range of interest in this thesis is only up to 100μm which corresponds to a voltage range of the sensors of approximately 1V (according to the sensor manufacturing data). This output voltage range of the sensors (0-1V) is too small to be a suitable input signal to the dSPACE ADC (analog-to-digital converter). 16-bit dSPACE ADCs, which have a voltage range of $\pm$10V, were used to record the output signals of the sensors. The resolution of the sensors (recorded by the ADCs) are reduced by a factor of 10 if the voltage range of the sensors of 1V is used instead of 10V. To improve the positioning resolution of the sensors, the output signals of these sensors were amplified; therefore a displacement range of interest (100μm) which corresponds to approximately 10V can be used to measure the displacements of the micro-motion stage. A conditioning amplifier (which was built at the electronics and instrumentation lab at the University of Adelaide) was used to amplify these signals. However, the amplifier may magnify the noise level which reduces the resolutions of the sensors. To determine the sensitivities and to quantify the resolutions of the eddy-current sensors, the measurement range of interest

of the sensors (100μm) were re-calibrated using a Michelson laser interferometer.

A Philtec D20 fibre-optic sensor was also used to measure the displacements of flexure hinges and to calibrate the sensitivities of strain gauges. The sensitivities of the fibre-optic sensor was investigated using the laser. The sensitivities of the fibre-optic sensor at its near and far sides obtained using the laser were compared with the sensitivities provided by the manufacturer (see Figures B.4 and B.5).

A.2 Aim

The aim of this experiment is to calibrate the sensitivities of the three eddy-current sensors and the fibre-optic sensor using a laser interferometer. It is also desired to quantify the resolutions and accuracies of the sensors by analysing measurement errors, system noise levels and the limitations of the equipment used.

A.3 Experimental Setup

A.3.1 dSPACE DS1104 controller board

A dSPACE DS1104 controller board consists of four 16-bit ADCs, four 12-bit ADCs and eight 16-bit DACs (digital-to-analog converters). All the ADCs and DACs have a voltage range of $\pm$10V. Analog input signals from sensors and photodiodes were connected to the four 16-bit ADCs to maximise the positioning resolution of the calibration results.

A.3.2 Sensor system - eddyNCDT3700

The eddyNCDT3700 package consists of three eddy-current sensors and two control circuits (a single and a dual-channel system). The eddyNCDT3700 is connected to a conditioning amplifier. The conditioning amplifier provides power and an additional amplifier for each sensor. It has an inbuilt analogue low-pass filter for each sensor. The amplifiers have a selective gain of 1, 5, 10, 20 or a variable gain adjusted with a potentiometer. Each amplifier also has two 'offset' adjustments via two potentiometers, one for coarse adjustment and one for fine adjustment. The maximum output voltage of the amplifier is approximately 14V. The analogue filters have a cut-off frequency of 1kHz. The output voltage range of the sensing system must be within -10V to +10V to be a suitable input to the dSPACE ADCs.

A.3.3 Fibre-optic sensor

A fibre-optic sensor (model D20), which is a product from PHILTEC, has a near side sensitivity of 12.046 μm/V and a far side sensitivity of -116 μm/V. These sensitivities were calibrated by PHILTEC in 2002. In order to ensure the accuracies of these sensitivities do not vary over time, the sensitivities were investigated here using the laser interferometer.

The following steps were carried out carefully when setting up the fibre-optic sensor. The sensor was arranged so that it was perpendicular to a target surface (which was a front surface mirror). Perpendicularity was established by positioning the sensor against the mirror while adjusting its contact angle (by turning an adjusting screw on a mirror housing) until a minimum voltage was read. For the best perpendicularity, the output voltage should be less than 250 mV as recommended by the manufacturer. The sensor was moved away by adjusting the translation stage until the maximum output level was attained. At that position, the GAIN controls (coarse and fine) were adjusted until the output voltage read 5 volts. The sensor gap was re-positioned to the desired operational set point, either at the near or the far side of the calibration graphs provided by the manufacturer (see Figures B.4 and B.5). The sensitivities of both sides were obtained using the laser interferometer in order to compare with the sensitivities provided by the manufacturer.

A.3.4 Michelson laser interferometer

The Michelson interferometer produces interference fringes by splitting a monochromatic beam so that one beam is directed to a movable mirror, M1 and the other to a fixed mirror, M2 (see Figure A.1). When they were brought back together, an interference pattern was formed. Fringes are only be obtained if the following steps are taken carefully.

Firstly, the distance of M1 and M2 to the back of the beam splitter was measured to be roughly the same (within a few millimeters). The photodiode shown in Figure A.1 was replaced temporarily with a screen for the ease of observing the fringes. Two pairs of images were seen, one reflected from the front surface of the beam splitter and the other reflected from its back surface. When the tilting screws on M2 were adjusted until one pair of images falls exactly on the other, the interference fringes were observed. Ideally, a set of concentric circular fringes should be observed if the perpendicularity between M1 and M2 was ensured. However, it was difficult to achieve absolute perpendicularity between the mirrors. A slight angular difference between the mirrors will allow us to observe localised fringes

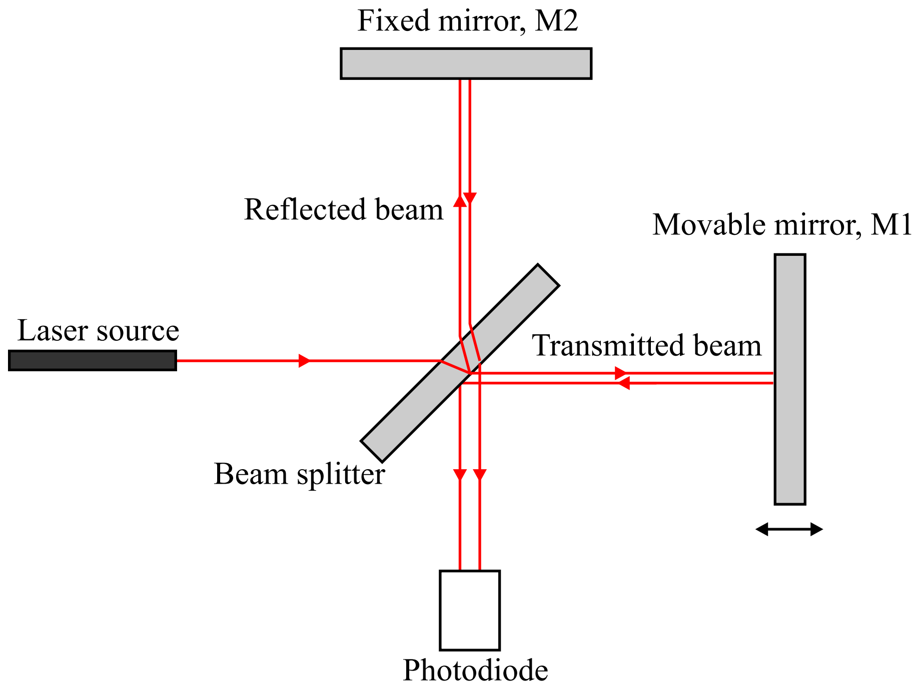

Figure A.1: Schematic of Michelson interferometer arrangement

instead (see Figure A.2). Fortunately, localised fringes were sufficient for these experiments as the interest of this experimental setup was to count the number of peaks from the intensity distribution of the interference fringes, and therefore to obtain the displacement of the movable mirror from the number of peaks counted.

Once the fringes were observed, the photodiode was placed into position to detect the intensity of the fringes. The intensity distribution of the fringes are shown in Figure A.3. The distance between two constructive interference maximum or minimum peaks was $\lambda/2$ because the beam travelled twice the distance when it was reflected from the mirrors. Displacements of the movable mirror were calculated by counting the number of constructive peaks. The displacement formulation of the movable mirror is,

$$d = (m + n - 1)\frac{\lambda}{4} \tag{A.1}$$

where d is the distance of the movable mirror, m is the number of maximum peaks, n is the number of minimum peaks, and λ is the wavelength of the laser.

The laser is a Helium-Neon (HeNe) type, which is a product of Uniphase (model number 1135P). It has a 632.8 nm wavelength and an output power of 20 mW. The output voltage of the photodiode was amplified by a gain of 10k to be a suitable input signal (between -10V to +10V) to the dSPACE ADC.

NOTE: This figure is included on page183 of the print copy of the thesis held in the University of Adelaide Library.

Figure A.2: Various types of fringes (Jenkins and White, 1981)

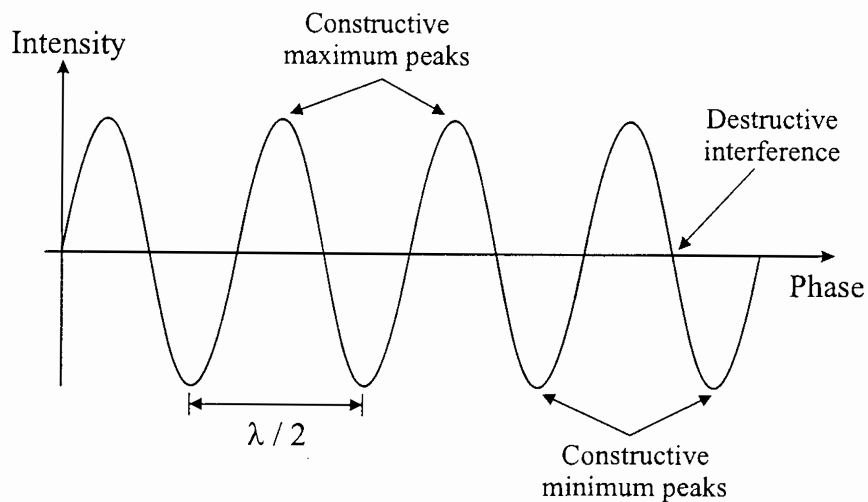

Figure A.3: Intensity distribution of interference fringes

A.3.5 Overall system setup

Aluminium targets of the eddy-current sensors were mounted on a NanoFlex^{TM} translation stage which is a product from Thorlabs (see Figure A.4). This stage has a travel range of 5 mm and a resolution of 50 nm. The displacements of the stage was motorised by connecting its differential adjuster to a DC motor via an O-ring (see Figure A.4). The 240VDC motor has a speed of 5 rev/min. The eddy-current sensors were mounted on a smaller translation stage (which is a product from Melles Griot). This stage has a travel range of 6 mm and a finest adjustment of 5 μm. It was used to position the eddy-current sensors to their corresponding measurement ranges of interest. The arrangement for fibre-optic sensor calibration was slightly different. The fibre-optic sensor was mounted on the NanoFlex^{TM} translation stage and its target (which was a front surface mirror) was mounted on a bracket as shown in Figure A.4.

The setup of the sensor calibration using the Michelson laser interferometer is shown in Figure A.5. An additional mirror was used to redirect the interference fringes onto the photodiode. The experiment was setup on an anti-vibration table with air-legs. The table was floated during experiments to minimise the low frequency vibrations (which could introduce noise during the laser measurement). The path of the laser beam was enclosed using a box to avoid influences of air current to the interference results during experiments.

For the calibration of the eddy-current sensors, signals of sensor 3316, 3317 and 3338 were connected to channels 1, 2 and 3 of the dSPACE ADCs respectively. Signals of the photodiode were connected to channel 4. For the calibration of the fibre-optic sensor, signals of the sensor were connected to channel 1. Sensors and laser signals were sampled at 5kHz.

A.4 Methods

A.4.1 Eddy-current sensors

The most linear region (measurement range of interest) of each eddy-current sensor was calibrated so that the inaccuracy due to linearity deviation will be minimised. Firstly, a graph of output voltage versus displacement of each sensor was obtained by moving the target (which was attached on the NanoFlex^{TM} translation stage) away from the sensor with an increment of 50 μm (until its measuring range, 1000 μm was reached) and the corresponding output voltage of the sensor was recorded. Figure A.6 shows the graph of output voltages versus displacements of each sensor.

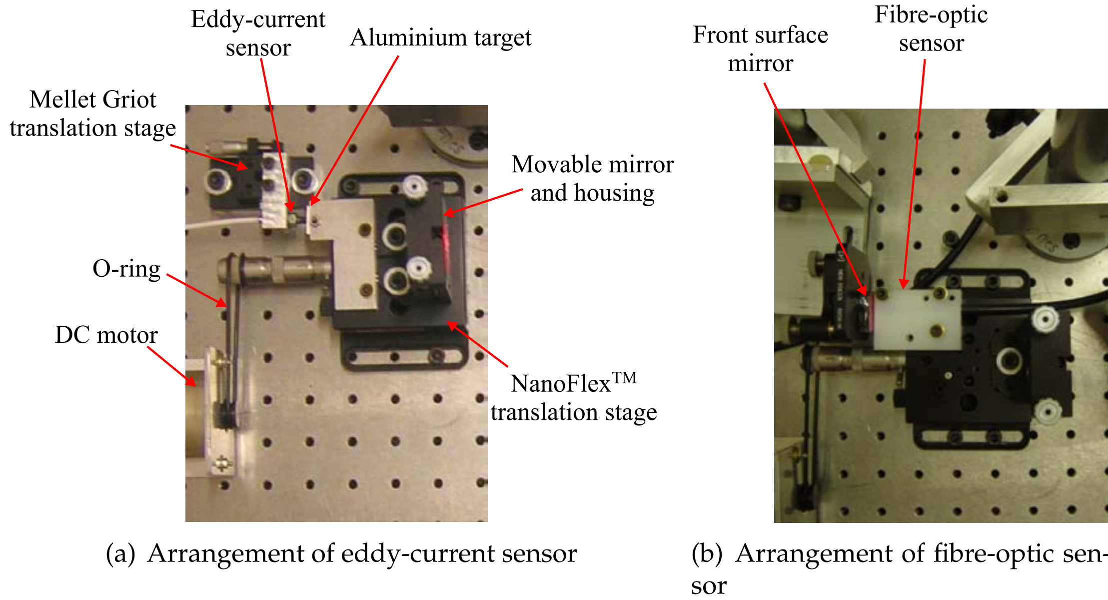

(a) Arrangement of eddy-current sensor

(b) Arrangement of fibre-optic sensor

Figure A.4: Attachment of sensor target and mirror on a motorised translation stage

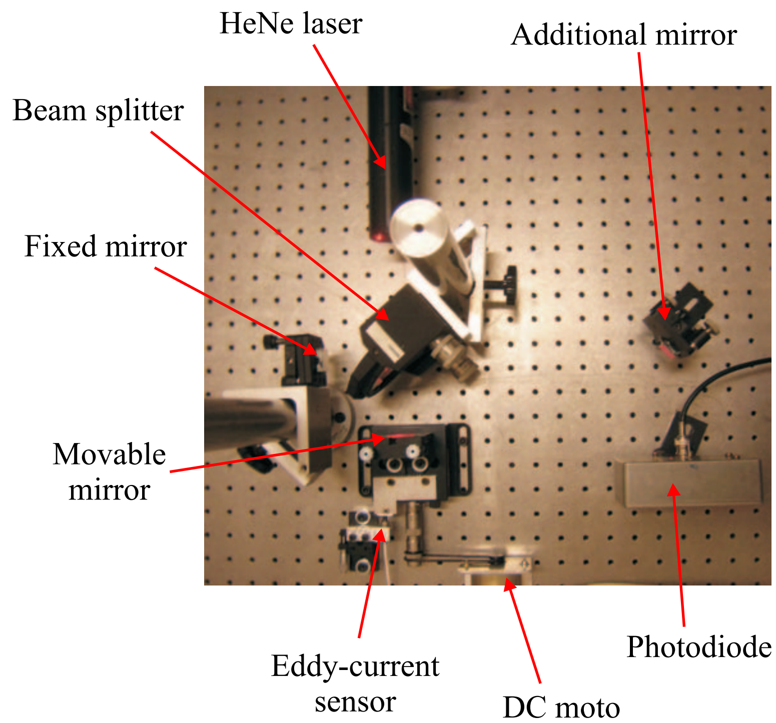

Figure A.5: Sensor calibration setup

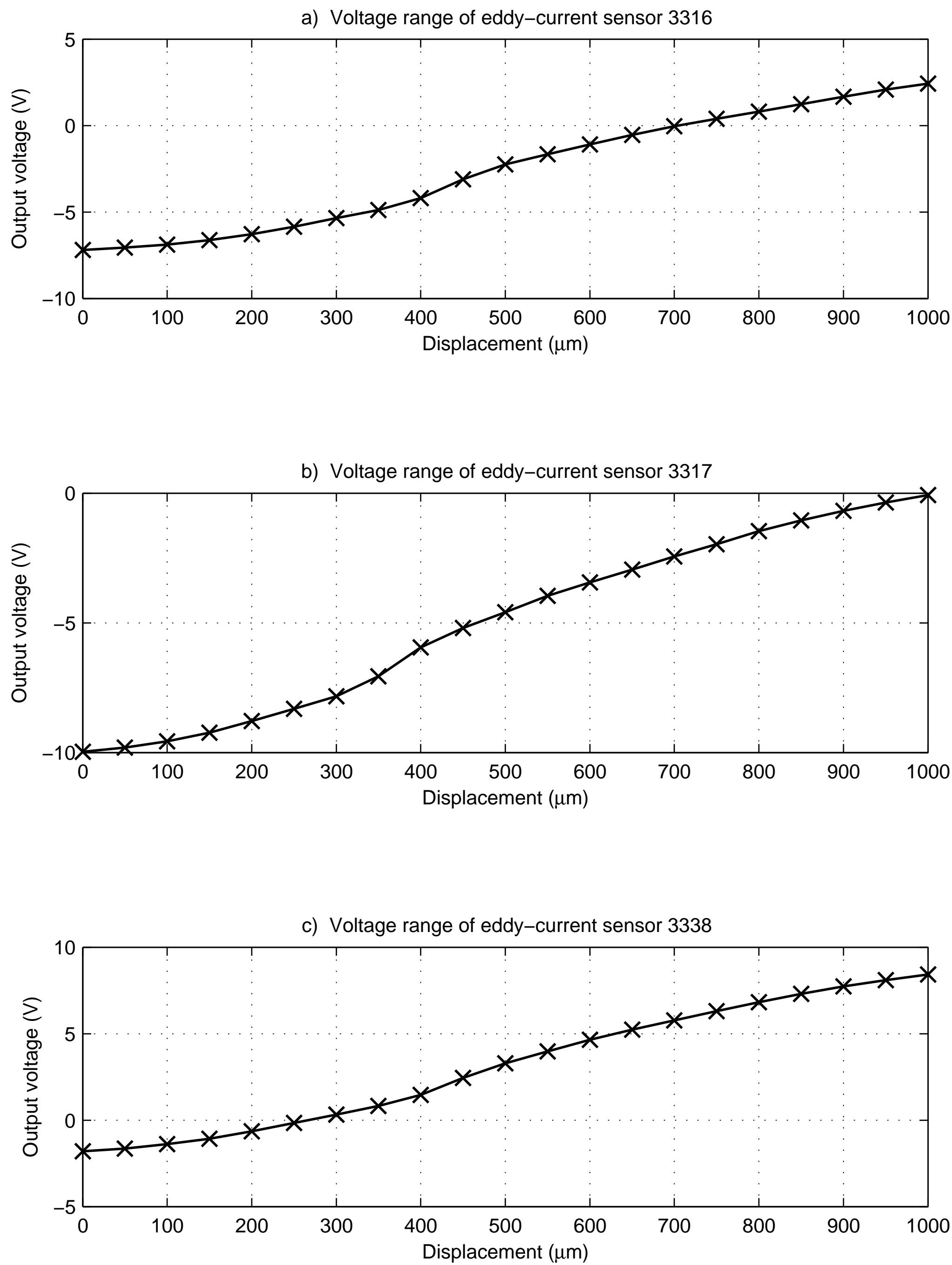

Figure A.6: Sensor output voltage versus displacement

Several linear regions were identified for each sensor by analysing Figure A.6. The linearity of each of these regions were further investigated. The target of each sensor was moved with an increment of 10 μm in these regions by adjusting the differential dial on the NanoFlex^{TM} stage and the corresponding output voltage was recorded. By comparing the linearity of these regions, the most linear region of each sensor was selected as the measurement range of interest. Figure A.7 shows the graph of output voltages versus displacements at the most linear region of each sensor.

The output voltage of each eddy-current sensor has to be within -10V to +10V to be a suitable input to the dSPACE ADCs. The variable gain and 'offset' of the conditioning amplifier were adjusted for each sensor so that the output voltages at their linear regions range from 0 to 10V.

Each eddy-current sensor was ensured to be located in its linear region before calibration data was taken by reading its output voltage (which was within 0 to 10V). The DC motor was turned on and the target of the sensor was moved slowly away from the sensor. The output voltages of the eddy-current sensor and the photodiode were recorded via the dSPACE ADCs. Twenty-five sets of calibration data were taken for each eddy-current sensor. Since the output voltages of sensor and photodiode were simultaneously sampled, the output voltages of eddy-current sensors could be extracted at the instant when a constructive peak was formed. The distance traveled by the NanoFlex^{TM} translation stage were calculated by using Equation A.1. The sensitivity of each eddy-current sensor was obtained by plotting distances travelled by the translation stage versus the output voltages of the sensors obtained at the instant when a peak was formed. Figure A.8 shows the sensitivity curves of each eddy-current sensor and their average sensitivities (change of displacements over change of voltages, $\Delta d/\Delta V$) obtained from the twenty-five sets of data.

A.4.2 Fibre-optic sensor

The procedure of calibrating the fibre-optic sensor was similar to the eddy-current sensors. Firstly, a linear voltage range of the sensor at the near side was identified, which was from 1.5V to 2.5V. This voltage range was sufficient to provide a measurement range of approximately 12 μm, which was sufficient to be used to measure the displacements of flexure hinges and to calibrate strain gauges. A set of calibration curves was obtained. It was noted that the sensitivity at the near side calibrated using the laser interferometer was different by about 0.3 μm/V compared to that of the manufacturer and the differences varied for different volt-

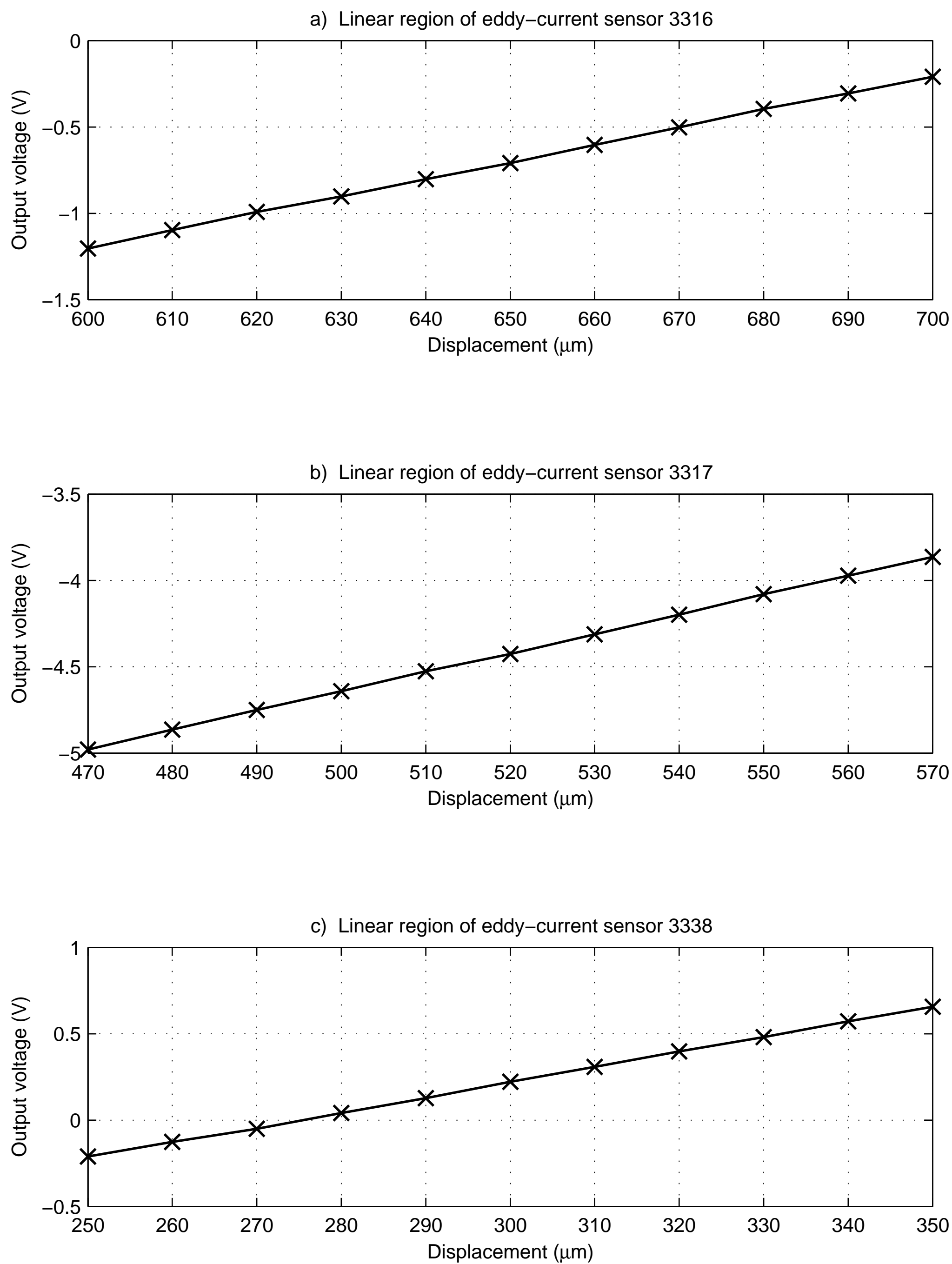

Figure A.7: Sensor output voltage versus displacement at the most linear region of eddy-current sensors

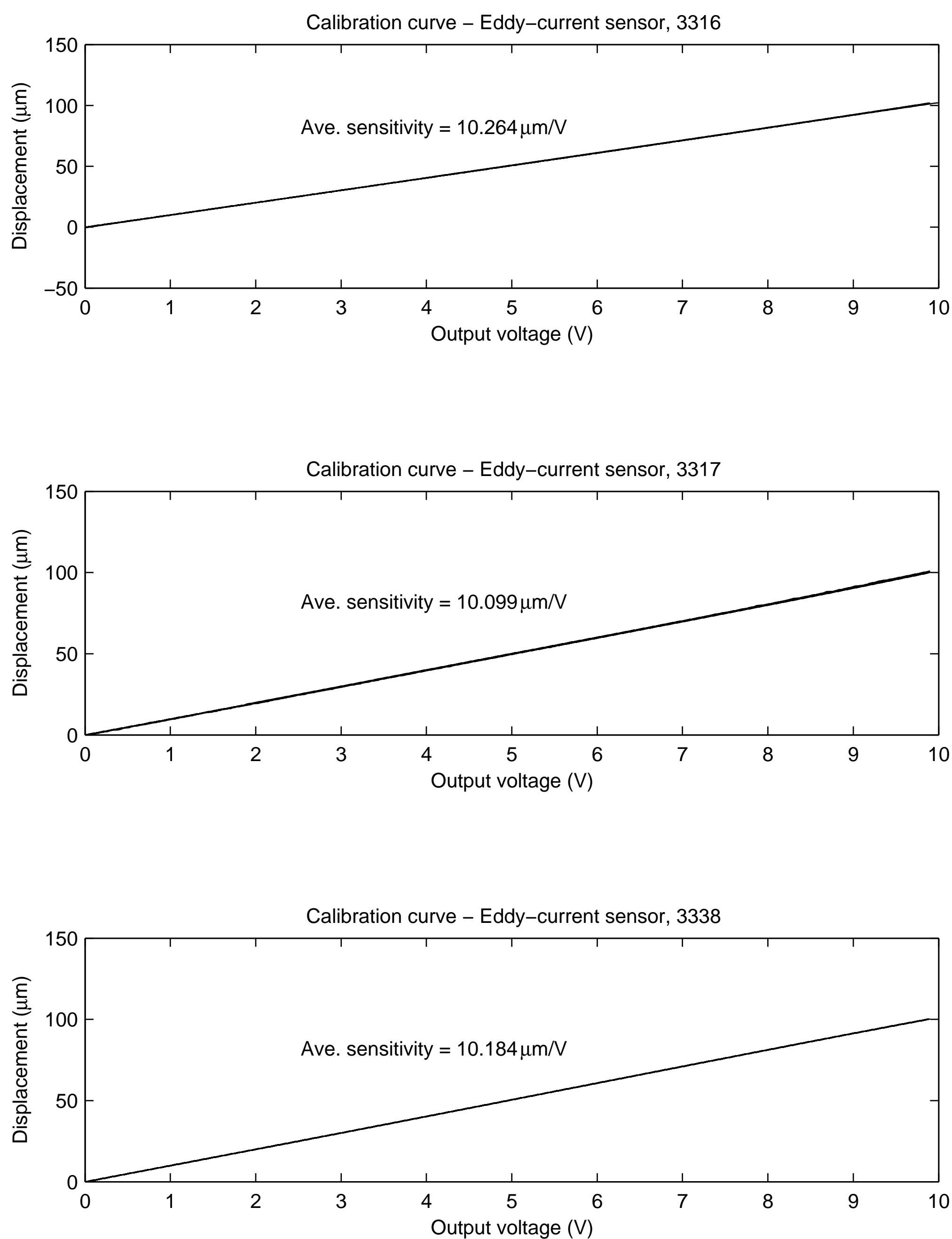

Figure A.8: Sensitivity curves of eddy-current sensors

age ranges. Therefore, a selected linear region (which was from 1.5V to 2.5V) was re-calibrated using the laser in order to obtain an accurate sensitivity for a measurement range of about 12 μm. Twenty-five sets of calibration data were taken. Figure A.9 shows the calibration curves of the sensor and its average sensitivity ($\Delta d/\Delta V$) obtained from the twenty-five sets of data.

The sensitivity of a linear voltage range of the fibre-optic far side was also investigated. Ten sets of data were taken and it was found the the sensitivities obtained from all the ten sets were consistent with that provided by the manufacturer. Therefore, it was concluded that the far side sensitivity provided by PHILTEC was still valid. No calibration was required for the far side sensitivity of this sensor.

A.5 Results

A.5.1 Estimation of sensor resolutions

A.5.1.1 ADC resolution

The output voltage range of the sensors and the photodiode must be within -10V to +10V to be a suitable input to the 16-bit dSPACE ADCs. The position resolution of the ADC is the displacement that corresponds to the least-significant-bit. The resolution of the sensor was approximated by multiplying the sensor sensitivity to the smallest voltage represented by the least-significant-bit. The ADC resolution is given by,

$$Res_{ADC} = \frac{\Delta d}{\Delta V} \times \frac{voltage\, range_{ADC}}{2^{16}} \tag{A.2}$$

The resolution of the ADC for each eddy-current sensor calculated using Equation A.2 is,

$$\begin{aligned} Res_{ADC\,3316} &= 10.264\mu m/V \times \frac{20V}{2^{16}} \\ &= 3.13\, nm \end{aligned}$$

$$\begin{aligned} Res_{ADC\,3317} &= 10.099\mu m/V \times \frac{20V}{2^{16}} \\ &= 3.08\, nm \end{aligned}$$

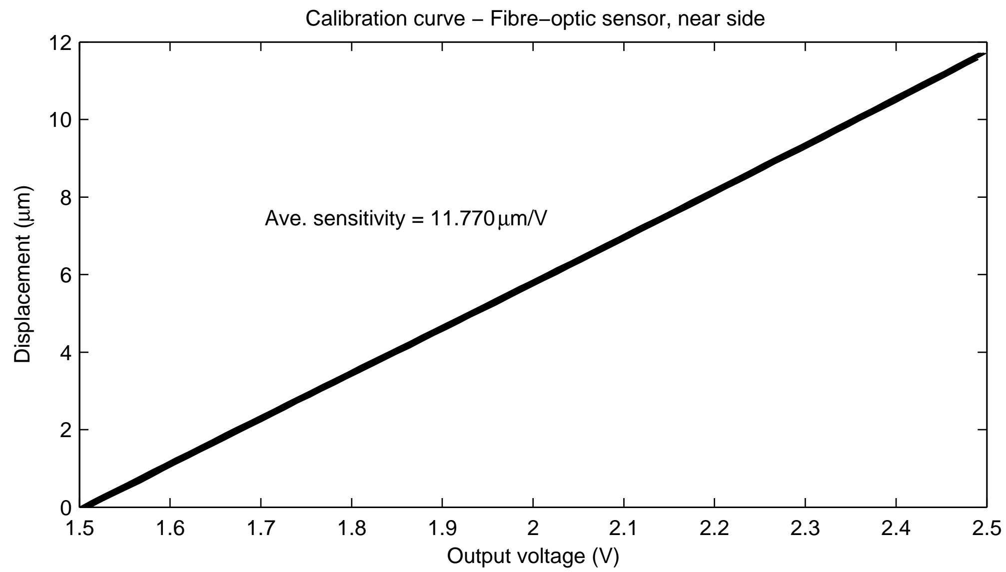

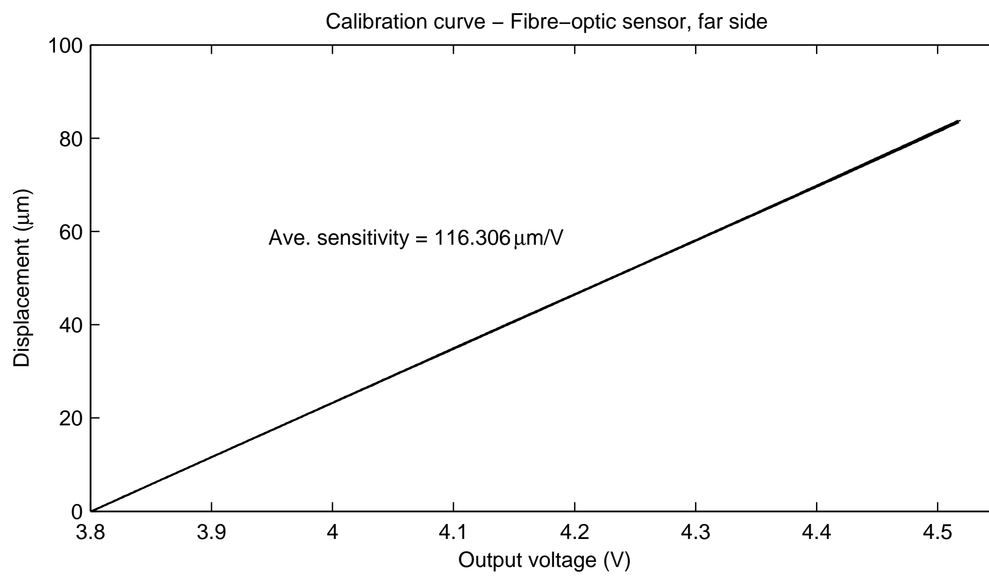

Figure A.9: Sensitivity curve of fibre-optic sensor

$$
\begin{aligned}
Res_{ADC\,3338} &= 10.184\mu m/V \times \frac{20V}{2^{16}} \\
&= 3.10\,nm
\end{aligned}
$$

The ADC resolution for the fibre-optic sensor calculated using Equation A.2 is,

$$
\begin{aligned}
Res_{ADC\,fibre-optic} &= 11.77\mu m/V \times \frac{20V}{2^{16}} \\
&= 3.59\,nm
\end{aligned}
$$

Sensitivities of the sensors, $\Delta d/\Delta V$ can be found in Figure A.8 and A.9.

A.5.1.2 Circuitry noise

Positioning resolutions of the sensors may be limited by signal noise. The noise of the sensors or circuitry was a small variation of voltages that could be mistaken for a position change. The magnitude of this voltage determined the smallest position change that can be recognised as a position change but not noise. The signal noise should be reduced as much as possible through an analog or digital filter. The conditioning amplifier has an inbuilt analog filter with a cut-off frequency of 1 kHz. The calibration results of the eddy-current sensors in this thesis will not be suitable for high frequency (more than 1 kHz) measurements*. The sensor signals were also filtered using a lowpass digital filter with 10 Hz cut-off frequency. The resolution of the sensors increased with the use of the lowpass digital filter. However it was only suitable for low frequency applications (below 10 Hz). The peak-to-peak voltage (V_{pp}) of each sensor was recorded when there was no displacement change between the sensor and target. The peak-to-peak voltage represents the noise of the voltage signals. When a digital filter was used, the peak-to-peak voltage (V_{pp}) recorded for each sensor was,

$$
\begin{aligned}
V_{pp(3316)} &= 1.8\,mV \\
V_{pp(3317)} &= 1.0\,mV \\
V_{pp(3338)} &= 1.5\,mV \\
V_{pp(fibre)} &= 0.3\,mV
\end{aligned}
$$

*This does not apply to the fibre-optic sensor. The operating frequency of the fibre-optic sensor is less than 200kHz

The positioning resolution of each sensor limited by the signal noise (with digital filtering) is,

$$Res_{noise} = V_{pp} \times \frac{\Delta d}{\Delta V}$$

$$\begin{aligned}
Res_{noise(3316)} &= 1.8mV \times 10.264\mu m/V = 18.5\,nm \\
Res_{noise(3317)} &= 1.0mV \times 10.099\mu m/V = 10.1\,nm \\
Res_{noise(3338)} &= 1.5mV \times 10.184\mu m/V = 15.3\,nm \\
Res_{noise(fibre)} &= 0.3mV \times 11.770\mu m/V = 3.5\,nm
\end{aligned}$$

When the sensor signal was unfiltered, the peak-to-peak voltage (V_{pp}) recorded for each sensor was,

$$\begin{aligned}
V_{pp\,non-filtered(3316)} &= 5\,mV \\
V_{pp\,non-filtered(3317)} &= 3.5\,mV \\
V_{pp\,non-filtered(3338)} &= 5\,mV \\
V_{pp\,non-filtered(fibre)} &= 4\,mV
\end{aligned}$$

The positioning resolution of each sensor limited by the signal noise (without digital filtering) is,

$$\begin{aligned}
Res_{noise\,non-filtered(3316)} &= 5mV \times 10.264\mu m/V = 51\,nm \\
Res_{noise\,non-filtered(3317)} &= 3.5mV \times 10.099\mu m/V = 35\,nm \\
Res_{noise\,non-filtered(3338)} &= 5mV \times 10.184\mu m/V = 51\,nm \\
Res_{noise\,non-filtered(fibre)} &= 4mV \times 11.770\mu m/V = 47\,nm
\end{aligned}$$

A.6 Error analysis

A.6.1 Measurement errors

Twenty-five sets of calibration data were obtained for each sensor. A linear graph was fitted to each set of the calibration data to find the slope (sensitivity) of the graph. The mean of the sensitivities was calculated for each sensor (displayed in

Sensor	Sample size	Mean $(\Delta d/\Delta V)$	Std. dev. σ	Max. deviation %
Eddy-current 3316	21	10.264	0.0022	0.04
Eddy-current 3317	22	10.099	0.0206	0.41
Eddy-current 3338	25	10.184	0.0015	0.03
Fibre-optic, near side	25	11.770	0.0045	0.08

Table A.1: Statistical values of each sensor calibration result

Figure A.8 and A.9). The standard deviation, σ of the sensitivity was calculated as below,

$$\sigma = \sqrt{\frac{1}{N-1}\sum_{i=1}^{n}(x_i - \overline{x})^2}$$

where N is the sample size.

Obvious outliers were removed manually from each data set. Therefore, each calibration data set of the sensors has slightly different sample sizes. Table A.1 summarises the statistical values of the calibration data for each sensor. The maximum deviation of the sensitivities of the sensors from the mean values was estimated using Equation A.3 below,

$$Max\,deviation = \frac{2\sigma}{(\Delta d/\Delta V)_{mean}} \times 100\,\% \tag{A.3}$$

A.6.2 Temperature effects

Electronic devices may be sensitive to the change of room temperature. The output voltages of the sensors drift with the change of room temperature; however these effects could be compensated by warming up the sensor system at least half an hour prior to experiments. The effect of the change of room temperature also leads to bias (offset) errors in the eddy-current sensors[†]. Figure A.10 shows the relationship between the temperatures and the output voltages of the sensors without the change of displacement between the sensors and the aluminium targets. The offset rates $(\Delta V/\Delta T)$ were approximately 89mV/°C, 82mV/°C and 159mV/°C for sensors 3316, 3317 and 3338 respectively. The sensor voltage ranges (0V to +10V) were

[†]Bias error of the fibre-optic sensor can be corrected by ensuring the maximum output voltage of the sensor to be 5V

calibrated at a constant room temperature of 22°C. If the sensors are operated at a different room temperature, the voltage range of the sensors need to be offset correspondingly. However, the maximum output voltage of the sensor exceeds +10V when the room temperature increases, which exceeds the maximum voltage range of the ADCs. As a result, the measurement range of the sensors is decreased. The maximum measurement range of each eddy-current sensor can be estimated using Equation A.4 when the room temperature increases to more than 22°C.

$$Measurement\,Range_{max} = \left[10V - \frac{\Delta V}{\Delta T} \times (temperature - 22^{\circ}C)\right] \times \frac{\Delta d}{\Delta V} \quad \text{(A.4)}$$

where the room temperature is in degree Celsius, and $\Delta d/\Delta V$ is the sensitivity of the sensors.

If a measurement range required for an experiment is less than 100 μm, it is advised to operate the eddy-current sensors in its "safe-voltage-range", which is approximately from +1.5V to +8.5V (corresponding to a measurement range of approximately 70 μm) to avoid errors attributed to the change of temperature. For maximum performance, the sensors needed to be operated within 22 to 22.5°C.

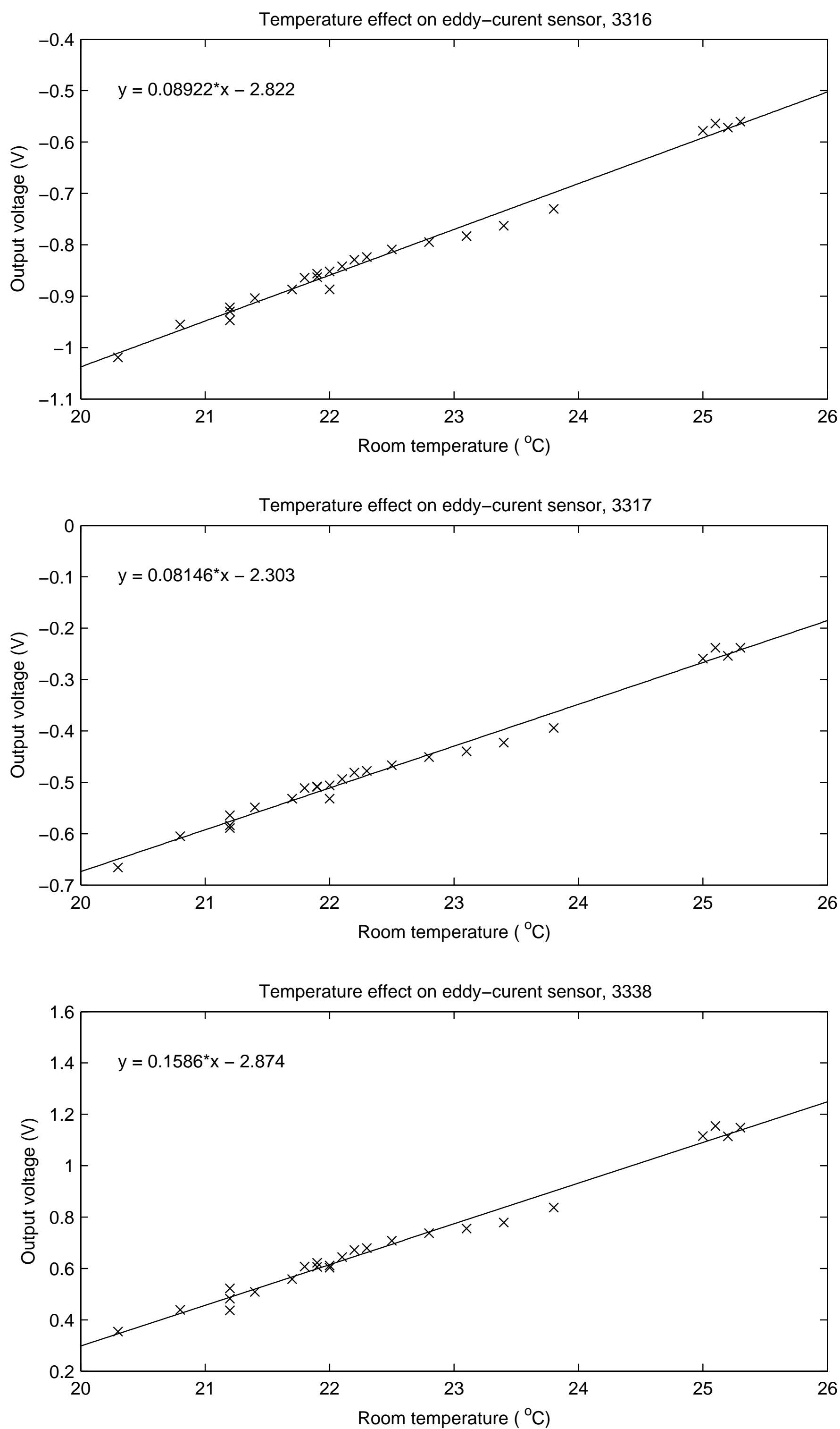

Figure A.10: Temperature effects on the eddy-current sensors

Sensors	Sensitivity , $\frac{\Delta d}{\Delta V}$	Max. deviation	Resolution (nm)		Measuring range (μm)	
	($\mu m/V$)	%	Filtered	Unfiltered	22 to 22.5°C	other °C
Eddy-current, 3316	10.264	0.04	18.5	51	102.6	use Eq. A.4
Eddy-current, 3317	10.099	0.41	10.1	35	101.0	use Eq. A.4
Eddy-current, 3338	10.184	0.03	15.3	51	101.8	use Eq. A.4
Fibre-optic, near side	11.770	0.08	3.5	47	11.77	11.77

Table A.2: Summary of the calibration results of the sensors

A.7 Summary

The calibration results and the resolution of the sensors in this thesis are accurate if the eddy-current sensors are operated at less than 1kHz and fibre-optic sensor is operated at less than 200kHz (without digital filtering); and the sensors are operated at less than 10Hz (with a 10Hz digital filter).

The eddy-current sensors have some limitations. The output voltages of the eddy-current sensors are shifted due to the change of room temperature. The distance between targets and sensors need to be adjusted prior to measurements; therefore the output voltage range of the sensors fall into the correct shifted voltage range. For example, if sensor 3316 is operated at 25°C, the distance between the sensor and the target need to be adjusted so that the starting voltage reads at 0.267V ($\Delta V/\Delta T \times (25°C - 22°C)$) instead of 0V. The maximum measurement range in this case will be about 99.9 μm (calculated using Equation A.4) instead of 102.6 μm. If a required measurement range is far less than 100 μm, it is advised to operate the eddy-current sensors in its “safe-voltage-range”, which is approximately from +1.5V to +8.5V (corresponding to a measurement range of approximately 70 μm) to avoid bias errors caused by the change of temperature. To achieve the optimum measurement range (which is $10V \times \Delta d/\Delta V$), the eddy-current sensors need to be operated within 22 to 22.5°C.

APPENDIX B

Manufacturing Data of Eddy-current and Fibre-optic sensors

NOTE: Appendix B is included in the print copy of the thesis held in the University of Adelaide Library.

APPENDIX C

Circular Flexure Hinge Compliance Equations

Paros and Weisbord (1965)

Full equations:

$\beta = t/2R$, $\gamma = 1 + \beta$, $\theta_m = \pi/2$ for right circular flexure hinge

$$\begin{aligned} \frac{\Delta\alpha_z}{M_z} &= \frac{3}{2EbR^2}\left[\frac{1}{2\beta+\beta^2}\right]\left\{\left[\frac{1+\beta}{\gamma^2}+\frac{3+2\beta+\beta^2}{\gamma(2\beta+\beta^2)}\right]\right. \\ &\quad \left[\sqrt{1-(1+\beta-\gamma)^2}\right]+\left[\frac{6(1+\beta)}{(2\beta+\beta^2)^{3/2}}\right] \\ &\quad \left.\left[tan^{-1}\left(\sqrt{\frac{2+\beta}{\beta}}\times\frac{(\gamma-\beta)}{\sqrt{1-(1+\beta-\gamma)^2}}\right)\right]\right\} \end{aligned} \tag{C.1}$$

$$\begin{aligned}\frac{\Delta y}{F_y} &= R^2 sin^2\theta_m \left(\frac{\alpha_z}{M_z}\right) - \frac{3}{2Eb}\left\{\left[\frac{1+\beta}{(1+\beta-cos\theta_m)^2}\right.\right. \\ &\quad \left. -\frac{2+\frac{(1+\beta)^2}{(2\beta+\beta^2)}}{(1+\beta-cos\theta_m)}\right] sin\theta_m \\ &\quad +\left[\frac{4(1+\beta)}{\sqrt{2\beta+\beta^2}} - \frac{2(1+\beta)}{(2\beta+\beta^2)^{3/2}}\right] \\ &\quad \left. \times tan^{-1}\sqrt{\frac{2+\beta}{\beta}} tan\frac{\theta_m}{2} - (2\theta_m)\right\}\end{aligned} \tag{C.2}$$

$$\begin{aligned}\frac{\Delta x}{F_x} &= \frac{1}{Eb}\left[-2tan^{-1}\frac{\gamma-\beta}{\sqrt{1-(1+\beta-\gamma)^2}}\right. \\ &\quad + \frac{2(1+\beta)}{\sqrt{2\beta+\beta^2}} tan^{-1}\left(\sqrt{\frac{2+\beta}{\beta}}\right. \\ &\quad \left.\left. \times \frac{\gamma-\beta}{\sqrt{1-(1+\beta-\gamma)^2}}\right)\right]\end{aligned} \tag{C.3}$$

Shear compliance: Shear modulus, $G = E/\left[2(1+\nu)\right]$

$$\begin{aligned}\left[\frac{\Delta y}{F_y}\right]_s &= \frac{1}{Gb}\left[-\theta_m + \frac{2(1+\beta)}{\sqrt{2\beta+\beta^2}}\right. \\ &\quad \left. \times tan^{-1}\sqrt{\frac{2+\beta}{\beta}} tan\frac{\theta_m}{2}\right]\end{aligned} \tag{C.4}$$

Simplified equations:

$$\frac{\alpha_z}{M_z} = \frac{9\pi R^{1/2}}{2Ebt^{5/2}} \tag{C.5}$$

$$\frac{\Delta y}{F_y} = \frac{9\pi}{2Eb}\left(\frac{R}{t}\right)^{5/2} \tag{C.6}$$

$$\frac{\Delta x}{F_x} = \frac{1}{Eb}\left[\pi (R/t)^{1/2} - 2.57\right] \tag{C.7}$$

Shear Compliance: Shear modulus, $G = E/\left[2\left(1+\nu\right)\right]$

$$\left[\frac{\Delta y}{F_y}\right]_s = \frac{1}{Gb}\left[\pi\left(R/t\right)^{1/2} - 2.57\right] \tag{C.8}$$

Smith *et al.* (1987)

$I_{zz} = 1/12bt^3$

$$\frac{\Delta\alpha_z}{M_z} = \frac{\left(1.13t/R + 0.332\right)R}{EI_{zz}} \tag{C.9}$$

Zhang and Fasse (2001)

$$\frac{\Delta\alpha_z}{M_z} = \left(-0.035 \times \frac{t}{2R} + 0.1109 \times \sqrt{\frac{t}{2R}}\right)^{-1} \tag{C.10}$$

Wu and Zhou (2002)

$s = R/t$

$$\begin{aligned}\frac{\Delta\alpha_z}{M_z} &= \frac{12}{EbR^2}\left[\frac{2s^3\left(6s^2+4s+1\right)}{\left(2s+1\right)\left(4s+1\right)^2}\right. \\ &\left. + \frac{12s^4\left(2s+1\right)}{\left(4s+1\right)^{5/2}} arctan\sqrt{4s+1}\right]\end{aligned} \tag{C.11}$$

$$\begin{aligned}\frac{\Delta y}{F_y} &= \frac{12}{Eb}\left[\frac{s\left(24s^4+24s^3+22s^2+8s+1\right)}{2\left(2s+1\right)\left(4s+1\right)^2}\right. \\ &+ \frac{\left(2s+1\right)\left(24s^4+8s^3-14s^2-8s-1\right)}{2\left(4s+1\right)^{5/2}} \\ &\left. \times \left(arctan\sqrt{4s+1}\right) + \frac{\pi}{8}\right]\end{aligned} \tag{C.12}$$

$$\frac{\Delta x}{F_x} = \frac{1}{Eb}\left[\frac{2\left(2s+1\right)}{\sqrt{4s+1}} arctan\left(\sqrt{4s+1}\right) - \frac{\pi}{2}\right] \tag{C.13}$$

Shear compliance: Shear modulus, $G = E/\left[2\left(1+\nu\right)\right]$

$$\left[\frac{\Delta y}{F_y}\right]_s = \frac{1}{Gb}\left[\frac{2\left(2s+1\right)}{\sqrt{4s+1}}\left(arctan\sqrt{4s+1}\right) - \frac{\pi}{2}\right] \tag{C.14}$$

Tseytlin (2002)

For thin circular hinges, t/R≤0.07

$$\frac{\Delta\alpha_z}{M_z} = 4\left\{1+\left[1+0.1986\left(\frac{2R}{t}\right)\right]^{1/2}\right\} / \left[Eb\left(\frac{t}{2}\right)^2\right] \tag{C.15}$$

The coefficient 0.1984 may be changed to 0.215 at angle $\theta_m \subseteq \pm 0.9$.

For intermediate circular hinges, 0.07<t/R≤0.2

$$\frac{\Delta\alpha_z}{M_z} = 4\left\{1+\left[1+0.373\left(\frac{2R}{t}\right)\right]^{1/2}\right\} / \left[1.45Eb\left(\frac{t}{2}\right)^2\right] \tag{C.16}$$

For thick circular hinges, 0.2<t/R≤0.6

$$\frac{\Delta\alpha_z}{M_z} = 4\left\{1+\left[1+0.5573\left(\frac{2R}{t}\right)\right]^{1/2}\right\} / \left[2Eb(\left(\frac{t}{2}\right)^2\right] \tag{C.17}$$

If Poisson's ration ν ≠0.333, multiply $\Delta\alpha_z/M_z$ by the factor $\left(1-\nu^2\right)/0.889$

Lobontiu (2003)

$$\frac{\Delta\alpha_z}{M_z} = \frac{24R}{Ebt^3\left(2R+t\right)\left(4R+t\right)^3}\left[t\left(4R+t\right)\right.$$

$$\left(6R^2+4Rt+t^2\right)+6R\left(2R+t\right)^2$$

$$\left.\sqrt{t\left(4R+t\right)}arctan\left(\sqrt{1+\frac{4R}{t}}\right)\right] \tag{C.18}$$

$$\begin{aligned} \frac{\Delta y}{F_y} &= \frac{3}{4Eb\left(2R+t\right)}\left\{2\left(2+\pi\right)R+\pi t\right. \\ &+\frac{8R^3\left(44R^2+28Rt+5t^2\right)}{t^2\left(4R+t\right)^2} \\ &+\frac{\left(2R+t\right)\sqrt{t\left(4R+t\right)}}{\sqrt{t^5\left(4R+t\right)^5}}\left[-80R^4+24R^3t\right. \\ &\left.+8\left(3+2\pi\right)R^2t^2+4\left(1+2\pi\right)Rt^3+\pi t^4\right] \\ &-\frac{8\left(2R+t\right)^4\left(-6R^2+4Rt+t^2\right)}{\sqrt{t^5\left(4R+t\right)^5}} \\ &\left.\times\left(arctan\sqrt{1+\frac{4R}{t}}\right)\right\} \end{aligned} \tag{C.19}$$

$$\frac{\Delta x}{F_x} = \frac{1}{Eb}\left[\frac{2\left(2R+t\right)}{\sqrt{t(4R+t)}}\left(arctan\sqrt{1+\frac{4R}{t}}\right)-\frac{\pi}{2}\right] \tag{C.20}$$

Shear compliance: Shear modulus, $G = E/\left[2\left(1+\nu\right)\right]$, α is shear correction factor

$$\left[\frac{\Delta y}{F_y}\right]_s = \frac{\alpha E}{G}\frac{\Delta x}{F_x} \tag{C.21}$$

Schotborgh *et al.* (2005)

$$\frac{\Delta\alpha_z}{M_z} = \left\{\frac{Ebt^2}{12}\left[-0.0089+1.3556\sqrt{\frac{t}{2R}}-0.5227\left(\sqrt{\frac{t}{2R}}\right)^2\right]\right\}^{-1} \tag{C.22}$$

$$\frac{\Delta y}{F_y} = \left\{Eb\left[0.0040-0.0727\sqrt{\frac{t}{2R}}+0.3417\left(\sqrt{\frac{t}{2R}}\right)^2\right]\right\}^{-1} \tag{C.23}$$

$$\frac{\Delta x}{F_x} = \left\{Eb\left[0.0010+0.4256\sqrt{\frac{t}{2R}}+0.0824\left(\sqrt{\frac{t}{2R}}\right)^2\right]\right\}^{-1} \tag{C.24}$$

Bibliography

ANSYS, 2002, ANSYS Element Reference, ANSYS Inc. *(Cited on page 34)*

Chang, S. H. and Du, B. C., 1998, 'A precision piezodriven micropositioner mechanism with large travel range', *Review of Scientific Instruments*, vol. 69, no. 4, pp. 1785–1791 *(Cited on page 20)*

Chang, S. H., Tseng, C. K. and Chien, H. C., 1999a, 'An Ultra-Precision XYθ_z Piezo-Micropositioner Part I: Design and Analysis', *IEEE Trans. Ultrasonics, Ferroelectrics, and Frequency Control*, vol. 46, no. 4, pp. 897–905 *(Cited on page 21)*

Chang, S. H., Tseng, C. K. and Chien, H. C., 1999b, 'An Ultra-Precision XYθ_z Piezo-Micropositioner Part II: Experiment and Performance', *IEEE Trans. Ultrasonics, Ferroelectrics, and Frequency Control*, vol. 46, no. 4, pp. 906–912 *(Cited on page 21)*

Choi, K.-B. and Kim, D.-H., 2006, 'Monolithic parallel linear compliant mechanism for two axes ultraprecision linear motion', *Review of Scientific Instruments*, vol. 77, pp. 065,106–1–7 *(Cited on page 29)*

Choi, K.-B. and Lee, J.-J., 2005, 'Passive compliant wafer stage for single-step nano-imprint lithography', *Review of Scientific Instruments*, vol. 76, no. 7, pp. 075,106–1–6 *(Cited on page 27)*

Choi, S., Han, S., Han, Y. and Thompson, B., 2006, 'A magnification device for precision mechanisms featuring piezoactuators and flexure hinges: Design and experimental validation', *Mechanism and Machine Theory* *(Cited on pages 28, 29, and 30)*

Chung, G., Yi, B.-J., Kim, W. and Chung, W., 2001, 'Design and Analysis of a Spatial 3-DOF Micromanipulator for Tele-operation', *Proceedings of the 2001 IEEE/RSJ,*

International Conference on Intelligent Robots and Systems, Maul, Hawaii, USA, pp. 337–342 *(Cited on page 23)*

Culpepper, M. L. and Anderson, G., 2004, 'Design of a low-cost nano-manipulator which utilizes a monolithic, spatial compliant mechanism', *Precision Engineering*, vol. 28, pp. 469–482 *(Cited on page 26)*

Elmustafa, A. A. and Lagally, M. G., 2001, 'Flexural-hinge guided motion nanopositioner stage for precision machining: finite element simulations', *Precision Engineering*, vol. 25, pp. 77–81 *(Cited on page 23)*

Furukawa, E. and Mizuno, M., 1990, 'Displacement Amplification and Reduction by Means of Linkage', *Bull. Japan Soc. of Prec. Engg*, vol. 24, no. 4, pp. 285–290 *(Cited on page 18)*

Furukawa, E., Mizuno, M. and Doi, T., 1995, 'Development of a Flexure-Hinged Translation Mechanism Driven by Two Piezoelectric Stacks', *JSME International Journal, Series C: Dynamics, Control, Robotics, Design and Manufacturing*, vol. 34, no. 4, pp. 743–748 *(Cited on pages 19 and 61)*

Gao, P., Swei, S. and Yuan, Z., 1999, 'A new piezodriven precision micropositioning stage utilizing flexure hinges', *Nanotechnology*, vol. 10, pp. 394–398 *(Cited on page 21)*

Gao, P. and Swei, S.-M., 1999, 'A six-degree-of-freedom micro-manipulator based on piezoelectric translators', *Nanotechnology*, vol. 10, pp. 447–452 *(Cited on page 21)*

Gao, P., Tan, H. and Yuan, Z., 2000, 'The design and characterization of a piezodriven ultra-precision stepping positioner', *Measurement, Science and Technology*, vol. 11, pp. N15–N19 *(Cited on page 22)*

Han, C., Tesar, D. and Traver, A., 1989, 'The Optimum Design of a 6 DOF Fully Parallel Micromanipulator for Enhanced Robot Accuracy', *ASME, Mechanical Systems Analysis, Design and Simulation, Advances in Design Automation*, vol. 19, no. 3, pp. 357–363 *(Cited on page 18)*

Han, C.-S., Hudgens, J., Tesar, D. and Traver, A., 1991, 'Modelling, synthesis, analysis, and design of high resolution micromanipulator to enhance robot accuracy', *IEEE/RSJ International Workshop on Intelligent Robots and Systems, IROS'91, Osaka, Japan*, pp. 1157–1162 *(Cited on page 18)*

Handley, D., Lu, T.-F. and Yong, Y. K., 2006, 'A simple and efficient modelling method for planar flexure hinge compliant mechanisms', *Accepted to be published in the Precision Engineering* *(Cited on page 29)*

Handley, D. C., 2006, The modelling and optimal design of a three degree-of-freedom XYθ_z micro-motion stage, Ph.D. thesis, The University of Adelaide *(Cited on pages vii, ix, 1, 18, 19, 29, 30, 152, 154, 155, 156, 157, 161, and 162)*

Her, I. and Chang, J. C., 1994, 'A Linear Scheme for the Displacement Analysis of Micropositioning Stages with Flexure Hinges', *Journal of Mechanical Design, Trans. ASME*, vol. 116, pp. 770–776 *(Cited on pages 10, 12, 16, and 19)*

Howell, L., 2001, Compliant Mechanisms, John Wiley & Sons, Inc. *(Cited on page 64)*

Hsiao, F.-Z. and Lin, T.-W., 2001, 'Analysis of a novel flexure hinge with three degrees of freedom', *Review of Scientific Instruments*, vol. 72, no. 2, pp. 1565–1573 *(Cited on page 22)*

Jenkins, F. A. and White, H. E., 1981, Fundamentals of Optics, Mc-GRAW-HILL *(Cited on pages x and 183)*

Jouaneh, M. and Yang, R., 2003, 'Modeling of flexure-hinge type lever mechanisms', *Precision Engineering*, vol. 27, pp. 407–418 *(Cited on pages 24, 29, and 30)*

Kim, D., Kang, D., Shim, J., Song, I. and Gweon, D., 2005, 'Optimal design of a flexure hinge-based XYZ atomic force microscopy scanner for minimizing Abbe errors', *Review of Scientific Instruments*, vol. 76, pp. 073,706–1–7 *(Cited on page 27)*

Kim, W.-K., Yi, B.-J. and Cho, W., 2000, 'RCC Characteristics of Planar/Spherical Three Degree-of-Freedom Parallel Mechanisms With Joint Compliances', *Journal of Mechanical Design*, vol. 122, pp. 10–16 *(Cited on page 122)*

Koseki, Y., Tanikawa, T. and Koyachi, N., 2002, 'Kinematic analysis of a translational 3-d.o.f. micro-parallel mechanism using the matrix method', *Advanced Robotics*, vol. 16, no. 3, pp. 251–264 *(Cited on page 24)*

Krovi, V., Ananthasuresh, G. and Kumar, V., 2002, 'Kinematic and Kinetostatic Synthesis of Planar Coupled Serial Chain Mechanisms', *Journal of Mechanical Design*, vol. 124, pp. 301–312 *(Cited on pages 5 and 75)*

Lee, C.-W. and Kim, S.-W., 1997, 'An ultraprecision stage for alignment of wafers in advanced microlithography', *Precision Engineering*, vol. 21, pp. 113–122 *(Cited on page 20)*

Liu, P. and Li, Q., 2002, 'Kinematics and dynamics of a general-purpose, parallel, compliant micromanipulator', *Proceedings of the I MECH E Part K: Journal of Multi-body Dynamics*, vol. 217, no. 1, pp. 39–50 *(Cited on page 25)*

Lobontiu, N., 2003, Compliant Mechanisms: Design of flexure hinges, CRC Press *(Cited on pages 10, 33, 34, 46, 47, 48, 49, 50, 99, 125, and 173)*

Lobontiu, N. and Garcia, E., 2003a, 'Analytical model of displacement amplification and stiffness optimization for a class of flexure-based compliant mechanisms', *Computers and Structures*, vol. 81, pp. 2797–2810 *(Cited on pages 25, 27, and 29)*

Lobontiu, N. and Garcia, E., 2003b, 'Two-axis flexure hinges with axially-collocated and symmetric notches', *Computers and Structures*, vol. 81, pp. 1329–1341 *(Cited on page 15)*

Lobontiu, N., Paine, J. S., Garcia, E. and Goldfarb, M., 2002a, 'Design of symmetric conic-section flexure hinges based on closed-form compliance equations', *Mechanism and Machine Theory*, vol. 37, pp. 477–498 *(Cited on pages 10, 15, and 16)*

Lobontiu, N., Paine, J. S. N., Garcia, E. and Goldfarb, M., 2001, 'Corner-Filleted Flexure Hinges', *Transactions of the ASME, Journal of Mechanical Design*, vol. 123, pp. 346–352 *(Cited on pages 10 and 14)*

Lobontiu, N., Paine, J. S. N., O'Malley, E. and Samuelson, M., 2002b, 'Parabolic and hyperbolic flexure hinges: flexibility, motion precision and stress characterization based on compliance closed-form equations', *Precision Engineering*, vol. 26, pp. 183–192 *(Cited on page 15)*

Lu, T.-F., Handley, D. C. and Yong, Y. K., 2004, 'Position Control of a 3 DOF Compliant Micro-Motion Stage', *The Eighth International Conference on Control, Automation, Robotics and Vision, ICARCV, Kunming, China*, pp. 1274–1278 *(Cited on pages ix and 160)*

Ma, H.-W., Yao, S.-M., Wang, L.-Q. and Zhong, Z., 2006, 'Analysis of the displacement amplification ratio of bridge-type flexure hinge', *Sensors and Actuators A*, , no. 2, pp. 730–736 *(Cited on page 27)*

Ohya, Y., Arai, T., Mae, Y., Inoue, K. and Tanikawa, T., 1999, 'Development of 3-DOF Finger Module for Micro Manipulation', *Proceedings of the 1999 IEEE/RSJ, International Conference on Intelligent Robots and Systems, Kyongju, South Korea*, pp. 894–899 *(Cited on page 22)*

Park, S. and Yang, S., 2005, 'A mathematical approach for analysing ultra precision positioning system with compliant mechanism', *Journal of Materials Processing Technology*, vol. 164-165, pp. 1584–1589 *(Cited on pages 26 and 29)*

Paros, J. M. and Weisbord, L., 1965, 'How to design Flexure Hinges', *Machine Design*, vol. 37, pp. 151–156 *(Cited on pages xi, 10, 11, 12, 13, 14, 16, 17, 19, 20, 27, 33, 34, 46, 47, 48, 49, 50, 99, 125, and 173)*

Pham, H. H. and Chen, I.-M., 2002, 'Kinematics, Workspace and Static Analyses of 2-DOF Flexure Parallel Mechanism', *7th International Conference on Control, Automation, Robotics and Vision (ICARCV'02), Singapore*, pp. 968–973 *(Cited on page 24)*

Pham, H.-H. and Chen, I.-M., 2005, 'Stiffness modeling of flexure parallel mechanism', *Precision Engineering*, vol. 29, pp. 467–478 *(Cited on pages 28 and 30)*

Pham, H.-H. and Chen, I.-M., 2006, 'Micromanipulation System Design Based on Selective Actuation Mechanisms', *The International Journal of Robotics Research*, vol. 25, no. 2, pp. 171–186 *(Cited on page 28)*

Pham, H.-H., Chen, I.-M. and Yeh, H.-C., 2005, 'Micro-motion selective-actuation XYZ flexure parallel mechanism: design and modeling', *Journal of Micromechatronics*, vol. 3, no. 1, pp. 51–73 *(Cited on pages 28 and 138)*

Rong, Y., Zhu, Y., Luo, Z. and Xiangxi, L., 1994, 'Design and analysis of flexure-hinge mechanism used in micro-positioning stages', *ASME, Production Engineering Division, Proceedings of the 1994 International Mechanical Engineering Congress and Exposition*, vol. 68, no. 2, pp. 979–985 *(Cited on pages 12 and 18)*

Ryu, J., Lee, S.-Q., Gweon, D.-G. and Moon, K., 1999, 'Inverse kinematic modeling of a coupled flexure hinge mechanism', *Mechatronics*, vol. 9, pp. 657–674 *(Cited on page 22)*

Ryu, J. W., Gweon, D. and Moon, K. S., 1997, 'Optimal Design of a Flexure Hinge Based XYθ Wafer Stage', *Precision Engineering*, vol. 21, pp. 18–28 *(Cited on pages 22, 27, 29, and 30)*

Ryu, J. W. and Gweon, D.-G., 1997, 'Error analysis of a flexure hinge mechanism induced by machining imperfection', *Precision Engineering*, vol. 21, pp. 83–89 *(Cited on pages 13 and 168)*

Schotborgh, W. O., Kokkeler, F. G., Tragter, H. and van Houten, F. J., 2005, 'Dimensionless design graphs for flexure elements and a comparison between three flexure elements', *Precision Engineering*, vol. 29, pp. 41–47 *(Cited on pages 15, 16, 33, 34, 46, 47, 48, 49, 50, 99, 125, 169, and 173)*

Scire, F. and Teague, E., 1978, 'Piezodriven 50-μm range stage with subnanometer resolution', *Review of Scientific Instruments*, vol. 49, no. 12, pp. 1735–1740 *(Cited on pages 17, 19, and 61)*

Shim, J., Song, S., Kwon, D. and Cho, H., 1997, 'Kinematic Feature Analysis of a 6-Degree-of-Freedom In-Parallel Manipulator for Micro-Positioning', *Proceedings of 1997 IEEE/RSJ International Conference on Intelligent Robots and Systems, Grenoble, France*, pp. 1617–1623 *(Cited on page 20)*

Smith, S., Chetwynd, D. and Bowen, D., 1987, 'Design and assessment of monolithic high precision translation mechanisms', *Journal of Physics E: Scientific Instruments*, vol. 20, pp. 977–983 *(Cited on pages 10, 11, 13, 14, 16, 33, 34, 46, 47, 48, 49, and 173)*

Smith, S. T., Badami, V. G., Dale, J. S. and Xu, Y., 1997, 'Elliptical flexure hinges', *Review of Scientific Instruments*, vol. 68, no. 3, pp. 1474–1483 *(Cited on pages xi, 10, 11, 13, 16, 17, 33, 45, 60, and 173)*

Tseytlin, Y. M., 2002, 'Notch flexure hinges: An effective theory', *Review of Scientific Instruments*, vol. 73, no. 9, pp. 3363–3368 *(Cited on pages 10, 11, 12, 14, 16, 33, 34, 46, 47, 48, 49, and 173)*

Wu, Y. and Zhou, Z., 2002, 'Design calculations for flexure hinges', *Review of scientific instruments*, vol. 73, no. 8, pp. 3101–3106 *(Cited on pages 10, 13, 33, 34, 46, 47, 48, 49, 50, 99, 125, and 173)*

Wu, Y. and Zhou, Z., 2004, 'An XYθ mechanism actuated by one actuator', *Mechanism and Machine Theory*, vol. 39, pp. 1101–1110 *(Cited on page 26)*

Xu, G. and Qu, L., 1996, 'Some Analytical Problems of High Performance Flexure Hinge and Micro-motion', *Proceedings of The IEEE International Conference on Industrial Technology, Shanghai, China*, pp. 771–775 *(Cited on pages 10 and 12)*

Xu, W. and King, T., 1995, 'Mechanical Amplifier Design for Piezo-actuator Applications', *IEE Colloquium on Innovative Actuators for Mechatronic Systems, London, UK*, vol. 170, pp. 1/1–1/5 *(Cited on pages 12 and 16)*

Xu, W. and King, T., 1996, 'Flexure hinges for piezoactuator displacement amplifiers: flexibility, accuracy, and stress considerations', *Precision Engineering*, vol. 19, pp. 4–10 *(Cited on pages 12 and 16)*

Yang, R., Jouaneh, M. and Schweizer, R., 1996, 'Design and characterisation of a low-profile micropositioning stage', *Precision Engineering*, vol. 18, pp. 20–29 *(Cited on pages 19, 24, and 61)*

Yi, B.-J., Chung, B. G., Na, H. Y. and Kim, K. W., 2003, 'Design and Experiment of a 3-DOF Parallel Micromechanism Utilizing Flexure Hinges', *IEEE Transactions on Robotics and Automation, Washington, DC, USA*, vol. 19, no. 4, pp. 604–612 *(Cited on page 25)*

Yong, Y. K., Lu, T.-F. and Handley, D., 2003, 'Loop Closure Theory in Deriving Linear and Simple Kinematic Model for a 3 DOF Parallel Micro-motion System', *Proceedings of SPIE on Device and Process Technologies for MEMS, Microelectronics, and Photonics III, Perth, Australia*, vol. 5276, pp. 57–66 *(Cited on page 61)*

Yu, J., Hu, Y., Bi, S., Zong, G. and Zhao, W., 2004, 'Kinematics feature analysis of a 3-DOF compliant mechanism for micro manipulation', *Chinese Journal of Mechanical Engineering*, vol. 17, no. 1, pp. 127–131 *(Cited on page 26)*

Zhang, S. and Fasse, E. D., 2001, 'A Finite-Element-Based Method to Determine the Spatial Stiffness Properties of a Notch Hinge', *Journal of Mechanical Design*, vol. 123, pp. 141–147 *(Cited on pages 10, 13, 16, 33, 34, 46, 47, 48, 49, and 173)*

Zhang, W. J., Zou, J., Watson, L. G. and Zhao, W., 2002, 'The Constant-Jacobian Method for Kinematics of a Three-DOF Planar Micro-Motion Stage', *Journal of Robotic Systems*, vol. 19, no. 2, pp. 63–72 *(Cited on page 23)*